Office of Satellite and Product Operations
Environmental Satellite Processing Center

Regional Advanced Baseline Imager and Visible Infrared Imaging Radiometer Suite Emissions Algorithm Theoretical Basis Document

Version 2.1

September 3, 2024

U.S. Department of Commerce
National Oceanic and Atmospheric Administration
National Environmental Satellite, Data, and Information Service
Office of Satellite and Product Operations

Authors

Shobha Kondragunta (NOAA/NESDIS/STAR)
Fangjun Li (South Dakota State University)
Xiaoyung Zhang (South Dakota State University)
Chuanyu Xu (IM Systems Group)

Changes/Revisions Record

This algorithm theoretical basis document is changed as required to reflect system, operational, or organizational changes. Modifications made to this document are recorded in the Changes/Revisions Record below. This record will be maintained throughout the life of the document.

Version Number	Date	Description of Change/Revision	Section/Pages Affected	Changes Made by Name/Title/ Organization
0.1	01/03/2023	First Draft	All	Shobha Kondragunta
1.0	04/17/2023	Final Draft	All	Shobha Kondragunta
2.0	10/25/2023	Draft	Some	Fanjun Li
2.1	09/03/2024	Cover page, Authors, Changes/Revisions Record, and Preface added to Version 2.0	Cover page, Authors, Changes/Revisions Record, Preface	Hannah Bowie, Technical Writer, ERT Inc.
2.1	09/03/2024	Quality Assurance	Cover page, Changes/Revisions Record, Preface	Clint Sherwood, Quality Assurance Manager, ERT Inc.

Preface

This document comprises the National Oceanic and Atmospheric Administration (NOAA) National Environmental Satellite, Data, and Information Service (NESDIS), Office of Satellite and Product Operations (OSPO), publication of this Regional Advanced Baseline Imager and Visible Infrared Imaging Radiometer Suite Emissions (RAVE) Algorithm Theoretical Basis Document (ATBD). This document reflects current operations for the DOC/NOAA/NESDIS Environmental Satellite Processing Center (ESPC) (NOAA5045) information technology systems. This document describes the established ESPC procedure for RAVE users in accordance with Federal, DOC, NOAA, NESDIS and OSPO requirements.

The published version of this document can be found at the OSPO SharePoint Products Library.

Contents

List of Tables

List of Figures

1. Introduction

1.1. Product Overview

1.1.1. Product Description

Regional Advanced Baseline Imager and Visible Infrared Imaging Radiometer Suite Emissions (RAVE) algorithm generates biomass burning (fire) emissions of carbon dioxide (CO_2), carbon monoxide (CO), fine particulate matter ($PM_{2.5}$), total particulate matter (TPM), sulfur dioxide (SO_2), organic carbon (OC), black carbon (BC), nitrogen oxides (NO_x), ammonia (NH_3), volatile organic compounds (VOCs), and methane (CH4) for every hour each day. Additionally, hourly mean fire radiative power (FRP) and, hourly fire radiative energy (FRE)are also provided. Fire emissions are provided on a 0.03° x 0.03° grid resolution and the area and the dominate land cover of each grid at which emissions are reported also provided in the output file. The product file is in netCDF4 format and the domain of interest is 3.5°N – 81.8°N and 144.96°E – 27.84°W (Figure 1).

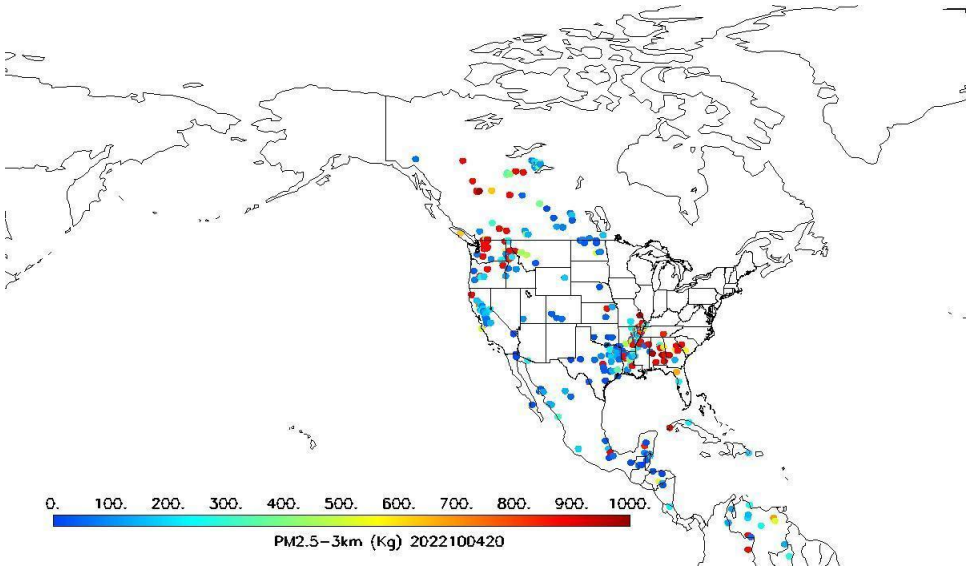

Figure 1: RAVE-North American domain is shown to illustrate the geographic area for which fire emissions are provided. In the figure, PM2.5 emissions for October 14, 2022 hour 20 are shown.

1.1.2. Product Requirements

The user (National Weather Service Environmental Modeling Center) has requested for fire radiative power, hourly emissions of $PM_{2.5}$, organic carbon, black carbon, methane, carbon dioxide, nitrogen dioxide, carbon monoxide, total particulate matter, volatile organic compounds, sulfur dioxide, and ammonia for the North American domain with a latency of one hour, refresh rate of one hour, a spatial resolution of 3 km, and a product accuracy of 20%.

1.2. Satellite Instrument Description

1.2.1. Data

1.2.1.1. Visible Infrared Imaging Radiometer Suite (VIIRS) active fire data

VIIRS onboard the sun-synchronous Suomi NPP and NOAA-20 satellites crosses the equator at 1:30 AM and 1:30 PM local time, but NOAA-20 VIIRS observes the same location approximately 50 minutes before or after Suomi NPP due to the half-orbit separation of the two satellites (Wolfe et al., 2013). VIIRS has a wide swath of 3000 km along the scan direction, which enables the instrument to observe the entire globe without gaps (Cao et al., 2014). VIIRS is equipped with a dedicated moderate resolution 4-µm band for fire monitoring (M13, 750 m) with a high saturation level to allow for FRP retrievals for the vast majority of fire pixels. Additionally, the imaging resolution (375m) I4 band provides better detection sensitivity and spatial detail, but limited potential for FRP retrievals due to its lower saturation. This band configuration led to the development of two active fire products: an M-band only heritage product (Csiszar et al. 2014), and an improved I-band / M-band hybrid product (Schroeder et al., 2014; hereafter referred to as the I-band product). Due to the onboard pixel aggregation and bow-tie deletion, VIIRS pixel size is generally more consistent across different scan angles from nadir to the scan edge and overlaps between consecutive scan lines are sharply reduced in comparison with Moderate Imaging Spectroradiometer (MODIS, Cao et al., 2014). This leads to relatively consistent fire detection capability in the full range of scan angles and negligible repeating detections of the same fire between scan lines (Li et al., 2020a; Li et al., 2018a). Because the VIIRS I-band can observe many more small fires (i.e., FRP ≥ 4 MW) relative to VIIRS M-band and MODIS (Fu et al., 2020; Li et al., 2020a, 2021a; Li et al., 2020c; Schroeder et al., 2014), we used the 375m VIIRS I-band active fire product in this study.

Defined in sensing geometry (or granule), for each fire detection, the VIIRS I-band L2 fire product provides observation time and location, FRP, satellite view zenith angle (VZA), solar zenith angle (SZA), persistent anomaly flag, and brightness temperatures in the 3.7 µm and 11 µm bands (Schroeder et al., 2020). Because of a low saturation temperature (367 K), the VIIRS 3.7 µm I4 band is saturated frequently over intense fires, hindering FRP calculation (Schroeder et al., 2014). Therefore, FRP for an I-band fire pixel is computed using the mid-infrared method (Wooster et al., 2005) with the co-located radiance in the 4-µm M13 band with a high nominal saturation temperature (634 K) (Csiszar et al., 2014; Schroeder et al., 2020). For the sake of simplicity, the 375m VIIRS I-band FRP is referred to as VIIRS FRP hereafter. The persistent anomaly flag in this product indicates that a fire pixel may correspond to a hot spot not associated with biomass burning, such as gas flares, volcanos, solar farms, urban, and other non-fire signals (Schroeder et al., 2020). Furthermore, the VIIRS I-band L2 fire product also provides a fire mask that classifies fire and non-fire (clear/cloudy) pixels.

For the correction of cloud impacts on FRP, the algorithm needs I-band geolocation product (namely GITCO) from Suomi NPP (NOAA-21 when it replaces Suomi NPP) and NOAA-20 VIIRS to locate cloud pixels from the fire mask.

1.2.1.2. Advanced Baseline Imager (ABI) active fire data

GOES-R ABI observes fires every 5 minutes across the CONUS and every 10 minutes over North and South Americas (full disk scan) in its current default operational mode, with a nominal pixel size of 2 km at nadir (Schmit et al., 2017). The first two GOES-R satellites - GOES-16 and GOES-17, positioned at 75°W and 137°W above the equator, have been running operationally since December 2017 and February 2019, respectively (Schmit et al., 2017). GOES-16 observes the CONUS from the east, with a VZA of 29° - 72°, while GOES-17 scans the CONUS from the west, with a VZA of 44° - 84°. The NOAA ABI active fire algorithm detects fires mainly using the 3.9 and 11.2 µm bands (Schmidt et al., 2012). For each fire detection, the ABI active fire product provides the observation location (coordinates) and time, FRP, fire flag, and the legacy instantaneous fire size and fire temperature estimates, which are not utilized in this study (Schmidt et al., 2012). FRP is calculated from the radiances in the 3.9 µm band and its accuracy for intense fires is improved because of the enhanced saturation temperature (411 K) of the ABI 3.9 µm band relative to legacy GOES satellites (Schmidt et al., 2012; Schmit et al., 2017). Fire detections are flagged into six groups: processed (good quality), saturated, cloud/smoke partially contaminated, high-, medium-, and low-probability (Schmidt et al., 2012). The first three categories indicate very confident detections that meet all algorithm tests while the other three categories suggest potential detections that only pass some of the algorithm tests. FRP is provided for all processed fires, most saturated, cloud contaminated, and high- and medium- possibility fires, and some low possibility fires.

The ABI L2 active fire product is generated in the ABI fixed grid projection. The projection defines the CONUS scan domain using 1500 by 2500 pixels. The product has been validated using the 30 m Landsat-8 and 375 m VIIRS fire detections and ground fire records across the southeast CONUS. The validation revealed that the ABI can observe low-intensity fires with an FRP as small as 34.5 MW confidently and fires that are missed by VIIRS due to obscuration of clouds or forest canopy (Li et al., 2020c). To remove false alarms, the algorithm preprocesses ABI fire detections using two strategies. First, because false alarms are mainly associated with fire detections masked as high, medium, and low possibility (Li et al., 2020c), only high/medium/low possibility fire pixels are considered if these pixels are also detected as processed and saturated fire detections at least once during a 24h window. Second, the algorithm uses two persistent anomaly masks (for both GOES-East and GOES-West) to remove false alarms related to gas flares, solar farms, urban, etc. The anomaly masks were generated using the persistent anomaly VIIRS fire pixels by NOAA VIIRS active fire product team.

1.2.1.3. Land cover and ecoregion maps

The RAVE algorithm uses land cover and ecoregion maps to classify fire detections and FRP for reconstructing FRP diurnal cycles. First, a 3 km land cover map was generated by aggregating vegetation classes from the 500 m MODIS land cover product in 2019 (Friedl et al., 2010). It consists of five main land cover types: (1) forest (including evergreen needleleaf and broadleaf, deciduous needleleaf and broadleaf, and mixed forests classes), (2) shrubland (including closed and open shrublands classes), (3) savannas (including savannas and woody savannas classes), (4) grassland (including grasslands and permanent wetlands classes), and (5) cropland (including croplands and cropland-natural vegetation mosaics classes). Second, a 3-km ecoregion map was generated from the Level I North America ecoregions developed by the United States Environmental Protection Agency (EPA, https://www.epa.gov/eco-research/ecoregions-north-america, last accessed on 12/01/2021). As a result, there are five main land cover types in 11 ecoregions (Figure 2).

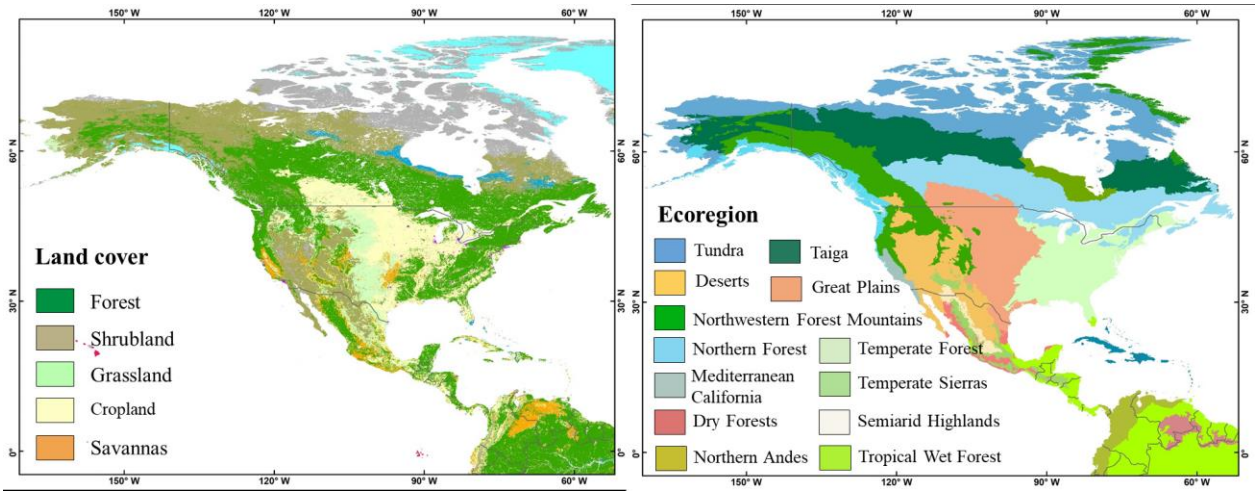

Figure 2: Land cover and ecoregions maps across the CONUS

2. Algorithm Description

2.1. Processing Outline

Provide a detailed outline of the retrieval algorithm's processing. Ensure all major elements and sub-elements needed to comprehensively understand the algorithm's processing are included in the outline. Include a data flow diagram consistent with the algorithm described in this section. As the software architecture matures, the level of detail contained in this section should also increase.

2.2. Algorithm Input

The RAVE algorithm depends on the operational polar-orbiting and geostationary satellite instruments that detect fires. Specifically, the Visible Infrared Imaging Radiometer (VIIRS) instruments on Suomi NPP (NOAA-21 when it replaces Suomi NPP) and NOAA-20 as well as the Advanced Baseline Imager (ABI) instruments on GOES-E and GOES-W satellites. Currently these are GOES-16 and GOES-17 but when GOES-18 replaces GOES-17, the RAVE algorithm should be able to switch over to using products generated from GOES-18 ABI. The RAVE algorithm also relies on some static input files such as climatological FRP diurnal cycles, climatological burn duration, emissions factors, land cover and ecoregion maps, and look-up-tables for VIIRS I-band pixel area. Table 1 below lists the products needed as input and provides an example name for the specific product.

Table 1: Input requirements for RAVE algorithm

Input File	**Sample File Name**
GOES-East ABI FD AF	OR_ABI-L2-FDCF-M6_G16_s20222721620209_e20222721629517_c20222721630071.nc
GOES-West ABI FD AF	OR_ABI-L2-FDCF-M6_G17_s20222721620321_e20222721629388_c20222721629536.nc or OR_ABI-L2-FDCF-M6_G18_s20230172330215_e20230172339523_c20230172340082.nc
GOES-East ABI FD CS mask	OR_ABI-L2-ACMF-M6_G16_s20222720640209_e20222720649517_c20222720651107.nc
GOES-West ABI FD CS mask	OR_ABI-L2-ACMF-M6_G17_s20222720640320_e20222720649387_c20222720650353.nc or OR_ABI-L2-ACMF-M6_G18_s20230172300215_e20230172309523_c20230172311094.nc
SNPP VIIRS I-band EFIRE	EFIRE-VIIRSI_v1r2_npp_s202207052353226_e202207052354468_c202309261342270.nc
NOAA-20 VIIRS I-band EFIRE	EFIRE-VIIRSI_v1r2_j01_s202207052354486_e202207052356113_c202309252221599.nc
SNPP VIIRS I-band geolocation	GITCO_npp_d20220929_t0056248_e0057489_b56589_c20220929023109906938_oebc_ops.h5
NOAA-20 VIIRS I-band geolocation	GITCO_j01_d20220929_t0059157_e0100384_b25192_c20220929013517310876_oebc_ops.h5
Static Input File	**Sample File Name**
Climatological FRP diurnal cycles	FRP_diurnal_climatology_10min_G2.csv burning_hours_csv
Climatological burn duration	burning_hours_climatology_G2.csv
emission factors	emission_factors_G2.csv
Lookup table of VIIRS I-band pixel area	viirs_iband_pixelarea_lut.csv
Maps of ecoregion and ecosystem	ecoregion_ecosystem_pt03degree_NorthAmerica_G2.bin
GOES-East mask of persistent false alarms	PA_RADF_G16_v2020Aug.nc
GOES-West mask of persistent false alarms	PA_RADF_G17_v2020Aug.nc
CMAQ model grid information	grid_spec_793.nc
Grid index for 13km data remapping	Grid_Index_4_13kmDataRemapping.txt
ESRI shapefile of North America maps	ne_50m_admin_0_countries.shp ne_50m_admin_1_states_provinces.shp ne_50m_coastline.shp

Emission scaling factors	emission_scaling_factors_new1.csv
GOES-West ABI geolocation lookup table	GOES_West_Lon_Lat_FD.bin
GOES-East ABI geolocation lookup table	GOES_East_Lon_Lat_FD.bin

2.3. Theoretical Description

2.3.1. Physical Description

The algorithm for hourly 3km emissions estimation proposed by this study is illustrated in Figure 3. The accuracy of the emission estimates was evaluated using the independent CO observations from S5P TROPOMI over selected fire events, and further compared with eight available biomass-burning emissions inventories.

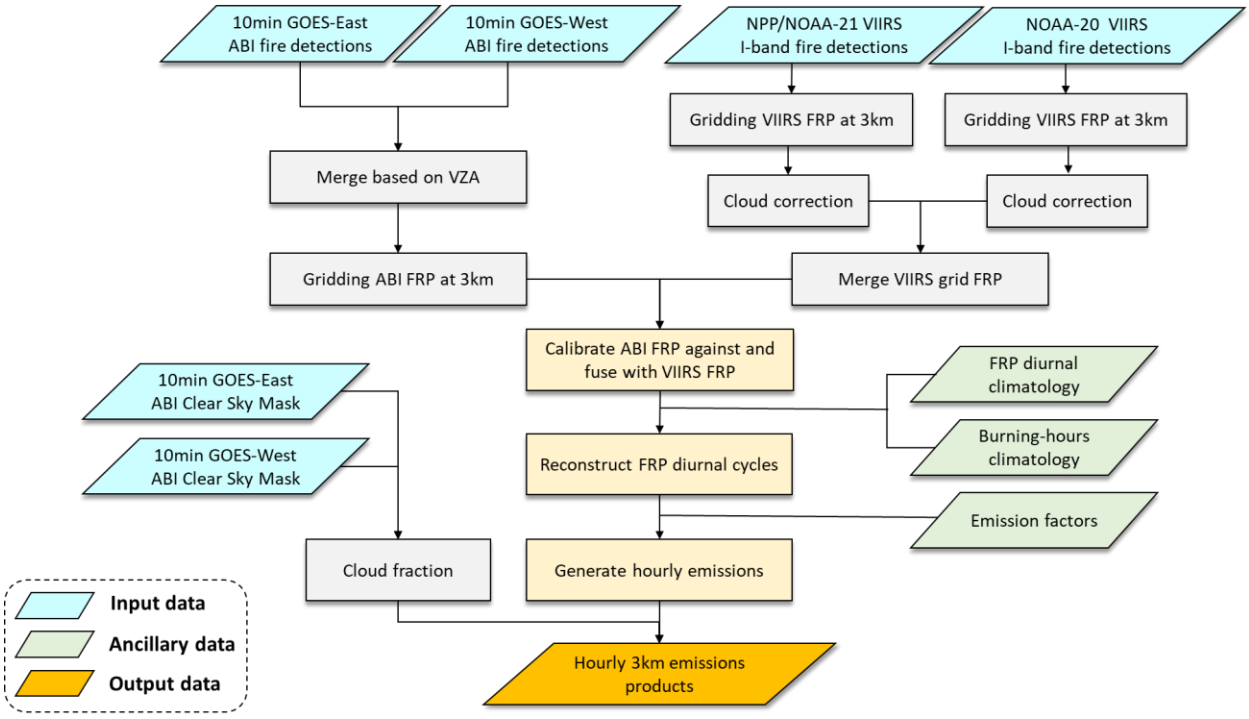

Figure 3: Flowchart of generating hourly 3 km emissions using ABI and VIIRS FRP. Note that the ABI and VIIRS fire detections are preprocessed data after removing false alarms based on a temporal filter and persistent anomaly flags.

2.3.1.1. Fusion of ABI FRP with VIIRS FRP

2.3.1.1.1. Gridding ABI and VIIRS FRP

ABI FRP from GOES-East (i.e. GOES-16) and GOES-West (i.e., GOES-17 or GOES-18) and VIIRS FRP from Suomi NPP and NOAA-20 were first merged and gridded at 3km separately. Because GOES-East and GOES-West observe fires across the North America simultaneously in opposite directions, ABI fire detections from the two satellites were merged based on satellite VZA. Before merging fire detections from two ABIs, ABI fire detections were preprocessed to correct terrain-related geolocation shift, known as the parallax error in ABI products defined in the ABI fixed grid projection, using two digital elevation model (DEM)-based geolocation lookup tables. To merge fire detections from two ABIs, specifically, for a given fire event observed by the two satellites at the same time, fire detections with smaller VZAs were selected. The merged fire detections have a VZA less than 60° (with a pixel area ≤ 9 km^2) in most areas of the CONUS and larger than 60° over high latitudes. The pixel-level FRP from legacy GOES satellites (e.g., GOES-13 and GOES-15) tended to be overestimated if a VZA was larger than 50° (Li et al., 2019) due to the contribution of non-fire background radiances (Schroeder et al., 2010). To examine if this issue also occurs in ABI FRP, we compared ABI FRP from GOES-16 and GOES-17 in four wildfires that occurred during the 2020 fire season in the western CONUS. For these fires, GOES-16 VZA varied from 53° to 64° (a pixel area of 7.6 - 9.6 km^2) and GOES-17 VZA changed very slightly between 46° and 50° (a pixel area of 6.3 – 6.9 km^2). We found that ABI FRP from the two satellites were comparable, with a small difference of 1% (Figure 4), which suggests that ABI FRP variation with VZA was negligible over the CONUS. Thus, the pixel-level FRP retrievals of the merged ABI fire detections that were observed at the same time and the same 3km grid were summed up, with each grid further classified by land cover and ecoregion maps. Note that the 3 km grids were mapped based on coordinates (i.e., longitude and latitude) with an interval of 0.03 degree. As a 3 km grid covered approximately 1 – 1.5 ABI pixels, we assumed that the grid was fully clear or totally cloudy if an ABI fire detection was provided with valid FRP retrieval (FRP > 0 MW) or was flagged as cloud contaminated, respectively. The cloud-contaminated detections were considered as temporal gaps with missing FRP values in the FRP diurnal cycle. Because ABI pixel area is greater than 9 km^2 in high latitudes, gridded ABI FRP in high latitudes is redistributed to 8-neighbor grids, weighted by VIIRS FRP in neighboring grids.

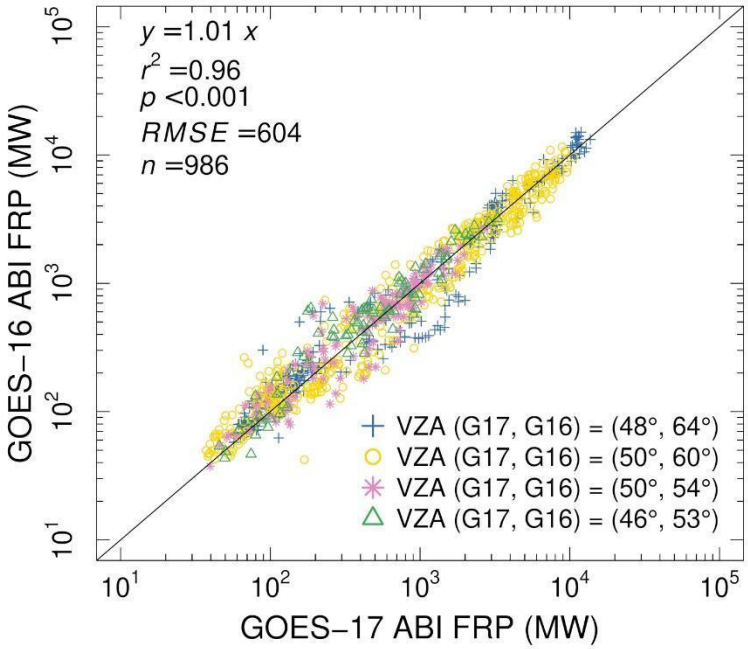

Figure 4: Comparison of GOES-16 and GOES-17 ABI FRP in four fires in 2020. Among these fires, GOES-17 VZA changed slightly between 46° and 50° while GOES-16 VZA varied largely from 53° to 64°, as shown in the VZA legend (for GOES-16). Each sample represents total FRP in a fire observed by both satellites at the same time.

The FRP at a 375 m pixel from Suomi NPP (or NOAA-21) and NOAA-20 VIIRS fire detections was also aggregated to 3 km grids based on the location of a VIIRS pixel center at each VIIRS overpass time separately, and further classified using the land cover and ecoregion maps. Because VIIRS could miss fire observations due to cloud obscuration, it is commonly assumed that fire burning condition under clouds is the same as that in clear-sky condition (Darmenov et al., 2015; Kaiser et al.; Giglio, 2007). However, this assumption of linear cloud correction could result in significant FRP overestimations if cloud fraction is very large. For the RAVE algorithm, the aggregated Suomi NPP and NOAA-20 VIIRS FRP for a given grid at an observation time was separately adjusted by assuming burning condition under clouds was non linearly correlated to the cloud fraction:

$$FRP^{V} = \frac{FRP^{V}_{agg}}{1-\beta+\alpha\times\beta^{2}} \quad (1)$$

where FRP^{V}_{agg} and FRP^{V} are the grid VIIRS FRP (unit: MW) before and after cloud correction; β is cloud fraction; and α is a coefficient that is set as 0.25 based on a set of tests. To further avoid FRP overestimation, cloud correction was not conducted in grids if the cloud fraction was larger than 95%. Then, the cloud-corrected grid VIIRS FRP from Suomi NPP (or NOAA-21) and NOAA-20 are merged based on observation times.

- **2.3.1.2. Calibrating and Fusing ABI FRP with VIIRS FRP**

The grid ABI FRP is calibrated against the grid VIIRS FRP because ABI FRP is potentially underestimated due to the omission of small and/or cool fires. This calibration is performed in a spatiotemporal-variant way using Eq. (2):

$$\overline{FRP_t^A} = FRP_t^A \times (1 + r) \tag{2}$$

where, at observation time *t*, FRP_t^A is the cloud-corrected grid ABI FRP (unit: MW, as in Eq. (1)); $\overline{FRP_t^A}$ is the calibrated grid ABI FRP using a calibration factor *r* (unitless).

The calibration factor r is computed using Eq. (3) based on the contemporaneous grid ABI and VIIRS FRP values by assuming that the ABI FRP underestimation is related to the magnitude of ABI FRP.

$$r = \frac{1}{n}\left(\frac{\sum_{i=1}^{n}\left(FRP_i^V - FRP_i^A\right)}{\sum_{i=1}^{n} FRP_i^A}\right) \tag{3}$$

where, for a given grid in a specific day, n denotes the total number of FRP pairs observed by both ABI and VIIRS contemporaneously (within ±5 minutes) during the day; FRP_i^V and FRP_i^A are the *i*th pair of the contemporaneous grid VIIRS FRP (cloud corrected) and grid ABI FRP, respectively.

The calibration factor r varies among grids and days; this has been demonstrated to be robust in improving the 2-km Himawari-8 AHI FRP relative to VIIRS FRP (Li et al., 2021a). Note that calibration factor cannot be computed when VIIRS FRP observations are not available at all in a given day due to obscuration of clouds or forest canopies or due to instrument anomalies. Although such cases are very few, we still developed fixed calibration factors to adjust ABI FRP. The constant factors are calculated using empirical relationships derived by comparing contemporaneous VIIRS FRP from Suomi NPP and NOAA-20 and GOES-16 ABI FRP over 100 fires that burned in 2020 across an ABI VZA range of 30° - 60° (Figure 4).

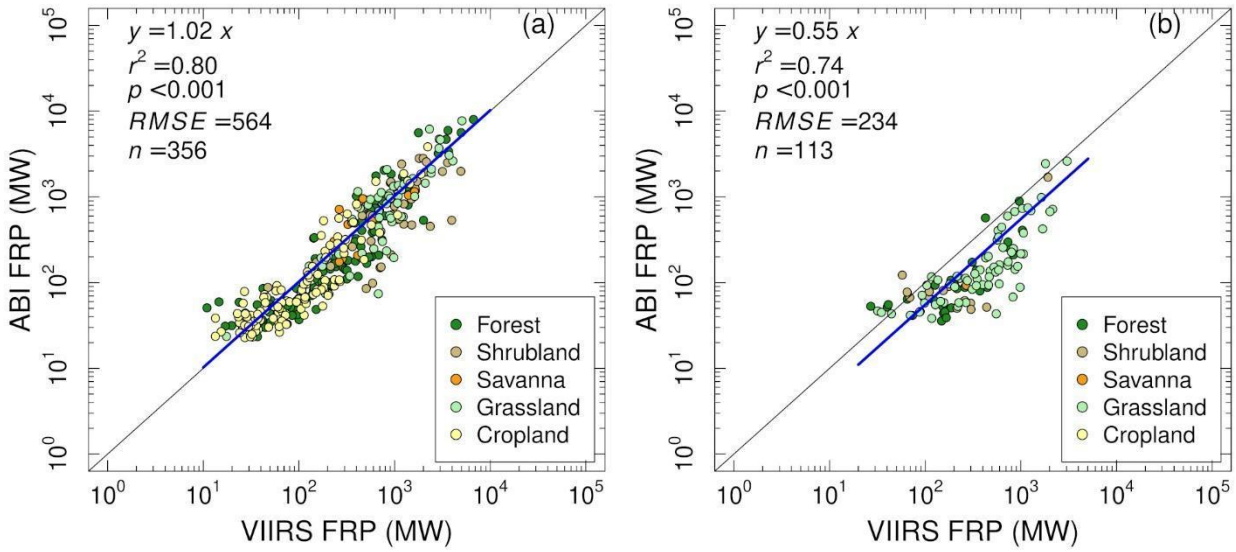

Figure 5: Comparison of contemporaneous ABI and VIIRS FRP in fire clusters. (a) Daytime and (b) nighttime. Each sample represents FRP observed by GOES-16 ABI and Suomi-NPP or NOAA-20 VIIRS contemporaneously (within ±2.5 min).

The calibrated grid ABI FRP and the grid VIIRS FRP were fused to generate ABI-VIIRS FRP time series as following:

$$FRP_t^f = w_1 \times FRP_t^V + w_2 \times \overline{FRP_t^A} \quad (4)$$

where for a given grid at observation time *t*, FRP_t^f, FRP_t^V, $\overline{FRP_t^A}$ are the fused ABI-VIIRS FRP, the cloud-corrected grid VIIRS FRP, and the calibrated ABI FRP (Eq.(2)), respectively; and w_1 and w_2 are weights to combine VIIRS and ABI FRP. When VIIRS FRP is available (with or without ABI FRP), w_1 = 1 and w_2=0; and when only ABI FRP is available, w_1=0 and w_2=1.

• 2.3.1.3. Reconstruction of FRP Diurnal Cycles

2.3.1.3.1. Building FRP Diurnal Climatologies

FRP diurnal climatologies were established to fit temporal gaps in the fused ABI-VIIRS FRP. As landscape-scale fire activities and characteristics (e.g., intensity, spread speed, and burning hours) are controlled by fuels, weather, and topography (Pyne et al., 1996), we built FRP diurnal climatologies for five main land cover types in 11 ecoregions using ABI FRP retrievals from GOES-16 from 2018-2020 and GOES-17 in 2020. An FRP diurnal climatology was established in three steps. First, for a given land cover type in a specific ecoregion, the gridded ABI FRP classified by land cover and ecoregion maps was binned every 5 minutes. Second, a mean FRP was calculated in each bin after removing a small number of outliers that were determined based on the density probability of FRP samples following Li et al. (2019). Third, the 5-minute mean FRP time series were fitted using the Discrete Fourier Transform (DFT) following

Giglio (2007) and Zhang et al. (2012). Note that when the number of ABI FRP samples was insufficient for a given land cover type in a specific ecoregion, the associated FRP diurnal climatology was not derived.

Figure 6 illustrates the derived land cover-ecoregion-specific FRP diurnal climatologies in 3km grids. Overall, all diurnal climatologies display a similar pattern, with decreasing FRP from midnight to early morning, then increasing and peaking between 12 PM and 4 PM, and then decreasing again gradually. Nevertheless, FRP diurnal climatology in the same ecoregion varies among five land cover types. For example, in deserts ecoregion, FRP climatologies are relatively larger with stronger variations in forest and savanna than other land cover types (Figure 6a). Further, FRP diurnal climatology in the same land cover type changes in FRP magnitude and peak time among different ecoregions. In forest, for example, climatological FRP is the largest in the forested mountains ecoregion and the smallest in the temperate forest ecoregion (Figure 6a); it peaks the latest the forested mountains ecoregion and the earliest in the temperate forest ecoregion (Figure 6b). Such large differences in climatological FRP are also observed in the croplands (Figure 6e, j). Among the five land cover types, the peak times of the FRP diurnal climatologies in Savanna are very close (Figure 6h).

Climatological burning hours or diurnal burning durations were also calculated for the same land cover type in a specific ecoregion to determine the possible fire burning length. Specifically, for a given land cover type in a specific ecoregion, the 5th and 95th percentiles of the observation hours in the density probability of FRP samples described above were calculated as the climatological start and end burning hours, respectively.

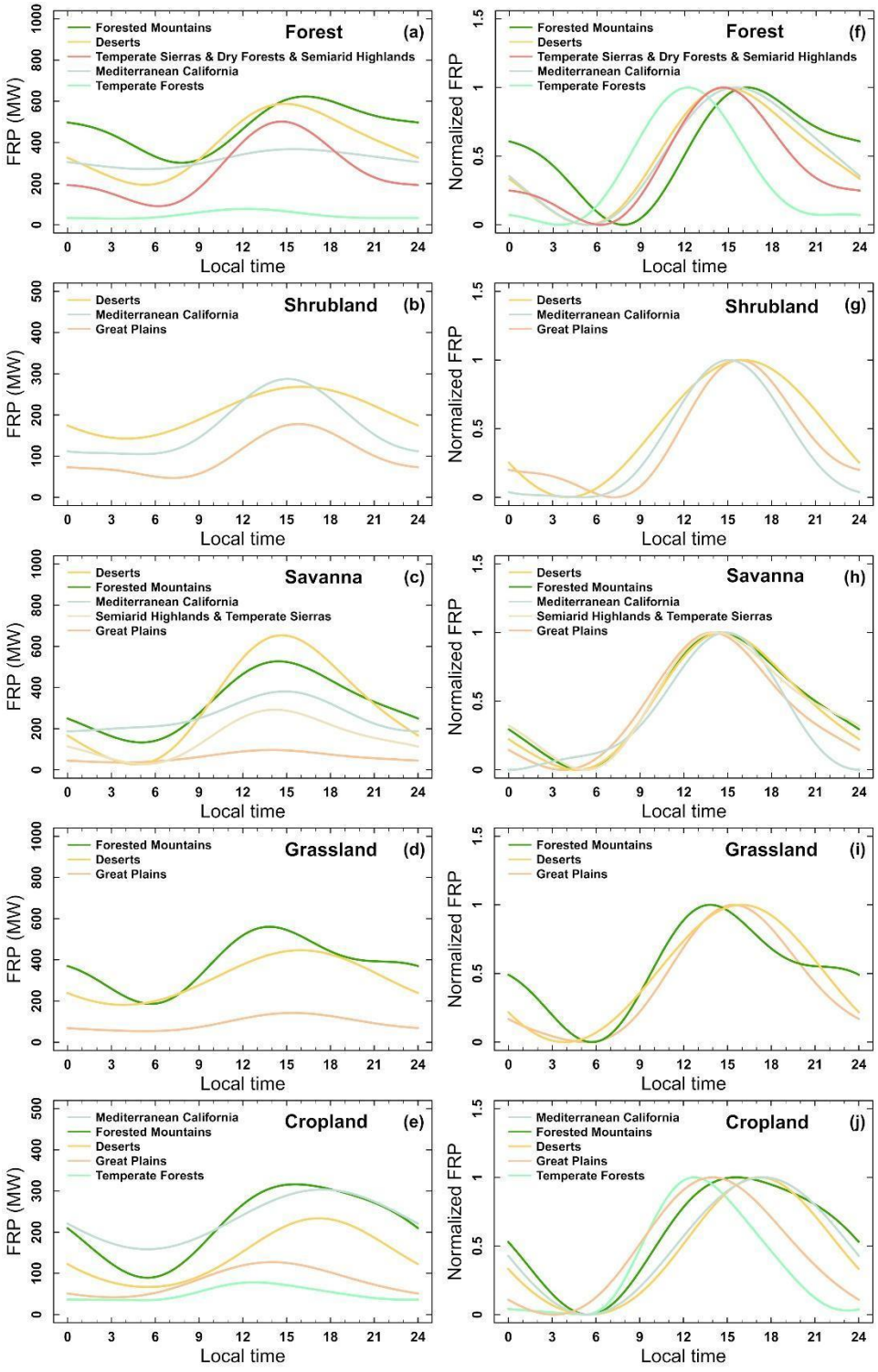

Figure 6: The land cover-ecoregion-specific FRP diurnal climatologies derived from GOES-16 and GOES-17 ABI FRP observations. The left column (a-e) shows the mean diurnal FRP in five land cover types: forest, shrubland,

savanna, grassland, and cropland; and the right column (f-j) shows the normalized FRP in the five land cover types, with a range 0 - 1.

2.3.1.3.2. Reconstructing FRP Diurnal Cycles

FRP diurnal cycles are reconstructed by filling temporal gaps in the fused ABI-VIIRS FRP time series. A temporal gap occurs when the sensors miss fire observations in specific hours or when the fire products fail to retrieve valid FRP for specific fire observations. Although the ABI instrument observes fires across North America every 10 minutes, it could miss fire observations in some observing times due to the obscuration of occasional clouds, very thick smoke plumes, and forest canopies. Of course, the instrument could have no fire observations at all in a specific grid if clouds fully cover the grid and persist all day, which can hardly be dealt with due to the lack of information on under-cloud burning conditions and thus is not considered in the following analyses. Furthermore, while FRP is sometimes provided by the ABI fire product for saturated pixels, the estimated FRP is known to be low and thereby has been considered an invalid FRP (or a temporal gap). The missing FRP in temporal gaps are predicted using the reconstructed FRP diurnal cycle. For a grid in which ABI and/or VIIRS observed fires during a specific day, an FRP diurnal cycle is reconstructed in two steps. First, temporal gaps, which refer to time slots when the valid ABI-VIIRS FRP is not available, are located. A gap could appear prior to or/and after a valid fused FRP; and its length could vary from a few minutes to several hours. Second, the missing FRP values in temporal gaps are predicted in two different ways. (1) For gaps shorter than one hour, missing FRP values are interpolated using the immediate neighboring valid FRPs. (2) Missing FRP values in gaps longer than one hour are predicted using FRP diurnal climatology, which is based on the assumption that FRP diurnal cycles share similar shapes for a given land cover type in the same ecoregion (Li et al., 2019; Zhang et al., 2012). Specifically, for a gap > 1h, the valid ABI-VIIRS FRP at each of the two ends of the gap are used to fit the associated, normalized climatological FRP diurnal cycle, respectively. The average of FRP values from the fitted diurnal climatologies at each observation time in the temporal gap is taken as predicted FRP missed in the gap. If without FRP values observed during a day but active fires are detected, the climatological FRP values are adopted. If FRP diurnal climatology is not available in the corresponding ecoregion, the climatology of the same land cover type from a neighboring ecoregion is used.

It is important to note that only parts of a given long gap are filled because fires might not burn continuously during the entire gap. For instance, fast-running grass or forest fires in the western CONUS could spread tens of kilometers in a day (Andela et al., 2019). In other words, those fires likely reside in a 3km grid only for several hours. Moreover, agricultural burnings and prescribed fires usually burn during some hours when fire weather is favorable and fires are manageable. Such fires could be very small and/or cool and detected by VIIRS only. Thus, we use the climatological burning hours (c.f. Section 3.2.1) to determine the possible burn duration of a long gap. We assume that fires burned two hours prior to and after a valid ABI-VIIRS FRP observation if a long gap occurs during climatological burning hours;

otherwise, a burning duration of one hour before and after a valid fused FRP observation is used. As a result, an FRP diurnal cycle in a 3 km grid consisted of the gap-filled fused FRP.

2.3.2. Estimation of Biomass-burning Emissions

The consumed dry matter and emitted fire emissions are computed from the reconstructed FRP diurnal cycles in 3km grids. For a given grid, hourly FRE is first calculated by integrating FRP diurnal cycle during each hour, as expressed in Eq. (5).

$$FRE = \int_{t1}^{t2} FRP_t^d \, dt \tag{5}$$

where FRE is hourly total FRE (unit: MJ); FRP_t^d is the 10-minute FRP value from the reconstructed FRP diurnal cycle (c.f. Section 3.2) at observation time *t*; and *t*1 and *t*2 denote the first and last 10-minute observation time slots in the given hour, respectively.

Then, hourly total dry matter consumption and emissions of eight chemical species (Table 2) are calculated for the RAVE product using equations 6 and 7 separately.

$$DM = FRE \times F_c \tag{6}$$

$$M_x = DM \times EF_x \tag{7}$$

where DM is hourly consumed dry matter (unit: kg); FRE is as in Eq. (5); F_c is the biomass combustion coefficient (unit: kg MJ^{-1}); M_x is hourly total mass (unit: kg) of emission species x; and EF_x is the emission factor (unit: kg kg^{-1}) of the species x.

FRE biomass combustion factors (F_c) in the CONUS wildfires was set as 0.368 kg MJ^{-1} that was obtained from field-based experiments (Wooster, 2005). The robustness of this value was verified in several laboratory and landscape measurements where the difference was less than 20% (Kremens et al., 2012; Li et al., 2018b; McCarley et al., 2020). Because RAVE algorithm is specific to the CONUS, emission factors (EF_x) are averaged from reported emission factor values for North American fires compiled in two recent emission factor datasets (Akagi et al, 2011; Andreae, 2019). Note that the global average value from Andreae (2019) was used directly if the number of studies for North America fires were less than three for a given species. The standard deviation (SD) was added to represent the EF uncertainty (Table 2).

Table 2. Emission factors (unit: g kg^{-1}) of eight chemical species

Emission species	Forest	Savanna, Shrubland, Grassland	Cropland
	mean (SD)	mean (SD)	mean (SD)
Carbon dioxide (CO2)	1598.5 (114)	1686.0 (112)	1585.0 (100)
Carbon monoxide (CO)	88.6 (22.2)	63.0 (14.7)	102.0 (33.0)
Particulate matter ($PM_{2.5}$)	12.8 (8.98)	7.17 (2.12)	6.26 (4.02)
Organic carbon (OC)	6.37 (3.30)	3.12 (0.92)	3.54 (3.34)
Nitrogen oxides (NO_x)	1.91 (1.82)	3.90 (1.50)	3.11 (1.57)
Ammonia (NH_3)	0.84 (0.72)	0.56 (0.53)	2.17 (1.27)
Sulfur dioxide (SO_2)	0.70 (0.48)	0.47 (0.44)	0.80 (0.42)
Total particulate matters (TPM)	18.4 (8.3)	8.7 (3.1)	12.9 (7.2)
olatile Organic Compounds (VOCs)	13.4 (11.8)	5.1 (5.9)	7.6 (8.6)
Black carbon (BC)	0.55 (0.40)	0.37 (0.20)	0.42 (0.28)
Methane (CH_4)	4.92 (2.8)	3.0 (2.2)	5.7 (6.0)

A set of biome-specific scaling factors are applied to three aerosol emission species (PM2.5, BC, and OC), producing scaled emissions estimates for these species. A temporal set of scaling factors is from the ones applied in the Quick Fire Emission Dataset (QFEDv2.5, Darmenov & Silva, 2015) and is to be updated soon in undergoing aerosol simulation experiments with RAVE emissions.

2.3.3. Mathematical Description

The entire description of the algorithm including mathematical description is given in Section 2.3.2. Some of the underlying assumptions and approximations are described in this section.
Assumptions: the algorithm assumes that diurnal profile of FRP over a certain biomass type is similar to climatological diurnal profiles.
Simplifications: the cloud correction approach is very simple. Currently there is no way to exactly know how FRP values are affected when thick smoke or cloud obscures the fires burning underneath. As a 3 km grid covered approximately 1 – 1.5 ABI pixels, we assumed that the grid was fully clear or totally cloudy if an ABI fire detection was provided with valid FRP retrieval (FRP > 0 MW) or was flagged as cloud contaminated, respectively. The RAVE algorithm treats ABI cloud-contaminated detections as temporal gaps with missing FRP values in the FRP diurnal cycle. The FRP at a 375 m pixel from Suomi NPP and NOAA-20 VIIRS fire detections is aggregated to 3 km grids based on the location of a VIIRS pixel center at each VIIRS overpass time separately, and further classified using the land cover and ecoregion maps. Because VIIRS could miss fire observations due to cloud obscuration, it is assumed that fire burning condition

under clouds is the same as that in clear-sky condition (Darmenov et al., 2015; Kaiser et al.; Giglio, 2007). However, this assumption of linear cloud correction could result in significant FRP overestimations if cloud fraction is very large. For the RAVE algorithm, the aggregated Suomi NPP and NOAA-20 VIIRS FRP for a given grid at an observation time is separately adjusted by assuming burning condition under clouds is non linearly correlated to the cloud fraction:

$$FRP^V = \frac{FRP^V_{agg}}{1-\beta+\alpha\times\beta^2} \quad (1)$$

where FRP^V_{agg} and FRP^V are the grid VIIRS FRP (unit: MW) before and after cloud correction; β is cloud fraction; and α is a coefficient that is set as 0.25 based on a set of tests. To further avoid FRP overestimation, cloud correction is conducted in grids if the cloud fraction is larger than 95%. Then, the cloud-corrected grid VIIRS FRP from Suomi NPP and NOAA-20 are merged based on observation times.

Approximations: Uncertainty in emission estimates could stem from biomass combustion coefficient (F_c in Eq.6). The algorithm uses a combustion coefficient (F_c) of 0.368 kg MJ^{-1} to convert FRE to dry matter in the RAVE product. This value was reported initially in a small field fire experiment (Wooster et al., 2005). Recent studies have further verified the usefulness of the coefficient: 0.298 kg MJ^{-1} in prescribed fires with oak as the primary fuel (Kremens et al., 2012); 0.4 kg MJ^{-1} based on lab experiment with western white pine needle as fuel when fuel moisture content is 10% (Smith et al., 2013); 0.32 kg MJ^{-1} based on Landsat-based fuel consumption and FRP from MODIS and legacy GOES at 445 wildfires across the CONUS (Li et al., 2018b); and 0.367 kg MJ^{-1} in two wildfires with complex fuel types using the airborne Lidar-based fuel consumption and MODIS FRP (McCarley et al., 2020). These studies indicate that the coefficient F_c varies within 18% of the initial value 0.368 kg MJ^{-1}, which could result in some uncertainty in the emissions estimates. Uncertainty in emission estimates could also arise from emission factor (EF_x in Eq.7). Emission factors depend strongly on combustion phase that is typically a mixture of smoldering and flaming phases (Christian et al., 2003; Liu et al., 2017; Prichard et al., 2020). As combustion transits from smoldering to flaming phase, emission factor decreases for most of fire emission species (e.g., CO_2, CO, and $PM_{2.5}$) but increases for a few species (e.g., NO_x and sulfate), with a change by severalfold (Liu et al., 2017; Yokelson et al., 2007). Moreover, emission factor also varies with fire types and fuel categories (Andreae, 2019; Liu et al., 2017; Prichard et al., 2020). To account for various fires for a given species, emission factors for a specific fuel (e.g., forest) are usually reported as the mean of available published values in many regions (Akagi et al., 2011; Andreae, 2019; Prichard et al., 2020). As the RAVE emissions focus on the North American domain, we used mean emission factors of reported values for fires in the temperate North America, which were extracted from the recently compiled emission factor datasets (Akagi et al., 2011; Andreae, 2019; Prichard et al., 2020). The influences of emission factors could be potentially bypassed using the emission coefficient that is a production of combustion coefficient and emission factor (Ichoku and Ellison, 2014; Lu et

al., 2019; Mota and Wooster, 2018). However, the emission coefficient is only available for a few species (e.g., total particulate matter or TPM and CO) (Ichoku and Ellison, 2014; Lu et al., 2019; Mota and Wooster, 2018), and it is very challenging to accurately determine.

2.4. Algorithm Output

The algorithm output is an hourly 3-km emissions file in netcdf format consisting of emissions of hourly FRP (mean and standard deviation), fire radiative energy, hourly cloud fraction, quality assurance flag (QA), FRP prediction flag, land cover type grid area, emissions of CO_2, CO, $PM_{2.5}$, BC, OC, NO_x, NH_3, SO_2, CH_4, TPM, VOCs, CH_4, a set of scaled estimates of these species, and metadata, as shown in Figure 7.

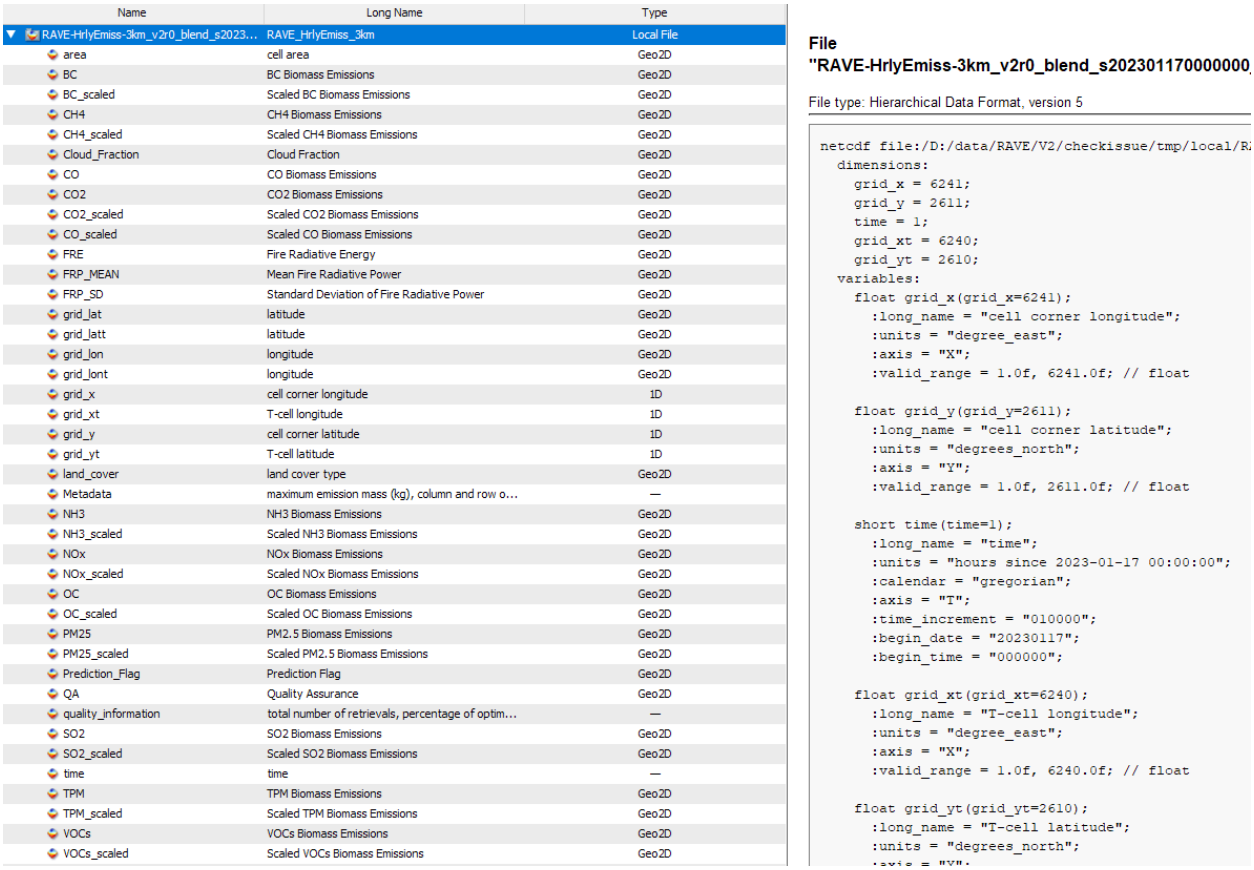

Name	Long Name	Type
RAVE-HrlyEmiss-3km_v2r0_blend_s2023...	RAVE_HrlyEmiss_3km	Local File
area	cell area	Geo2D
BC	BC Biomass Emissions	Geo2D
BC_scaled	Scaled BC Biomass Emissions	Geo2D
CH4	CH4 Biomass Emissions	Geo2D
CH4_scaled	Scaled CH4 Biomass Emissions	Geo2D
Cloud_Fraction	Cloud Fraction	Geo2D
CO	CO Biomass Emissions	Geo2D
CO2	CO2 Biomass Emissions	Geo2D
CO2_scaled	Scaled CO2 Biomass Emissions	Geo2D
CO_scaled	Scaled CO Biomass Emissions	Geo2D
FRE	Fire Radiative Energy	Geo2D
FRP_MEAN	Mean Fire Radiative Power	Geo2D
FRP_SD	Standard Deviation of Fire Radiative Power	Geo2D
grid_lat	latitude	Geo2D
grid_latt	latitude	Geo2D
grid_lon	longitude	Geo2D
grid_lont	longitude	Geo2D
grid_x	cell corner longitude	1D
grid_xt	T-cell longitude	1D
grid_y	cell corner latitude	1D
grid_yt	T-cell latitude	1D
land_cover	land cover type	Geo2D
Metadata	maximum emission mass (kg), column and row o...	—
NH3	NH3 Biomass Emissions	Geo2D
NH3_scaled	Scaled NH3 Biomass Emissions	Geo2D
NOx	NOx Biomass Emissions	Geo2D
NOx_scaled	Scaled NOx Biomass Emissions	Geo2D
OC	OC Biomass Emissions	Geo2D
OC_scaled	Scaled OC Biomass Emissions	Geo2D
PM25	PM2.5 Biomass Emissions	Geo2D
PM25_scaled	Scaled PM2.5 Biomass Emissions	Geo2D
Prediction_Flag	Prediction Flag	Geo2D
QA	Quality Assurance	Geo2D
quality_information	total number of retrievals, percentage of optim...	—
SO2	SO2 Biomass Emissions	Geo2D
SO2_scaled	Scaled SO2 Biomass Emissions	Geo2D
time	time	—
TPM	TPM Biomass Emissions	Geo2D
TPM_scaled	Scaled TPM Biomass Emissions	Geo2D
VOCs	VOCs Biomass Emissions	Geo2D
VOCs_scaled	Scaled VOCs Biomass Emissions	Geo2D

- **Figure 7: List of RAVE output parameters**

2.5. Performance Estimates

2.5.1. Test Data Description

The RAVE algorithm was tested on the data for October 2022 to ensure that the performance is identical between the research version and operational version. The regression test was successful with 100% agreement between the outputs generated from the science code and operational code.

2.5.2. Sensor Effects

Sensor characteristics such as calibration and saturation temperatures at the 3.9 um band do impact fire detection and FRP estimates. The RAVE algorithm only uses fire product retrievals with good confidence and therefore any data artifacts present in the fire products do not creep into fire emissions products. The RAVE algorithm also uses persistent anomaly flags to remove false fire detections associated with solar farms.

2.5.3. Retrieval Errors

Retrieval errors in emissions occur at large view and solar zenith angles due to uncertainties associated with FRP values, especially for GOES ABI. These retrievals are assigned a lower quality flag and users are advised to use the data with lower quality flags with caution. Table 3 lists the quality flag descriptions. ABI fire detections also have parallax errors that are not corrected. Fires appear at wrong geolocation when they are detected in high latitudes when GOES-East or GOES-West satellites observe the fires with large view angles.

Table 3: RAVE quality flag description

Quality Flag	Description
High	• Hours when ABI and/or VIIRS have confident fire observations (i.e., the "Processed" category for ABI) in clear-sky condition (for both fire grid and 8 neighboring grids)
Medium	• Hours when "High" class (above) spatially neighboring to more than one cloudy grid (determined based on "cloud fraction" information). • Hours when with saturated/cloudy/smoky ABI fire detections. • Hours when high/medium/low possibility in ABI fire detection, with

	fires detected by VIIRS during the past 24 hours. • Hours when predicted FRP (from climatology) temporally neighboring to the “high” or “medium” quality class from above.
Low	• Hours with medium/low possibility in ABI fire detections and without VIIRS fires during past 24 hours • Hours with predicted FRP from climatology • Open shrub and barren grids where only ABI observed fires (without VIIRS fire detections) during past 24 hours (false alarms in ABI fire detections frequently occur in the southwest CONUS) • Grids where both GOES-16 and GOES-17 ABI’s view zenith angle > 60° • Solar zenith angle (80° < SZA < 90°)

2.6. Practical Considerations

2.6.1. Numerical Computation Considerations

One of the hurdles of depending on upstream level 2 products is that if there are any production errors, they will carry over to the fire emissions product. The active fire algorithm runs slowly when it is unable to derive background temperature and the process at times is slow leading to drop out of granules. In that situation, when a particular VIIRS granule does not have fire detections, then we cannot calibrate ABI fire emissions accurately. The algorithm depends on climatological correction factors to fix ABI FRP values.

2.6.2. Programming & Procedural Considerations

Provide all programming and procedural information related to the implementation of the numerical model as operating code.

2.6.3. Quality Assessment & Diagnostics

Describe the following information concerning the quality of both output products and retrievals:

- Assessment of quality
  The quality of output products is described qualitatively using quality assurance (QA, Table 3). The unitless QA includes three confidence classes: low, medium, and high, with corresponding QA values of “1”, “2”, “3”. Fill value is denoted by “-1”.
- Documentation
- Any anomalies diagnosed

If there is any additional quality assessment or diagnostic information associated with the algorithm, please provide it in this section.

2.6.4. Exception Handling

2.7. Validation

There are two approaches to validation of RAVE. One aspect of validation is to evaluate the FRP values by intercomparing with other correlative measurements such as from other satellites or aircraft observations during field campaigns. The second approach is to use RAVE carbon monoxide (CO) emissions to compare with Tropospheric Monitoring Instrument (TROPOMI) CO observations.

FRP observations from the FIREX-AQ field campaign were used to evaluate RAVE FRPs. Figure 8 shows MODIS Airborne Simulator observations of Williams Flats fire on August 3, 2019 with GOES-16 ABI pixels of fire detections overlaid. Because airborne observations are at 20m resolution, the fire front and the flaming/smoldering fire pixels can be seen at high resolution. Six GOES-16 ABI pixels were observed to have fires detected at the time of aircraft flight. While the fires detected by ABI fall into the fire front/regime, the aircraft in situ FRP value is 23% higher than RAVE FRP value. Table 4 lists all the flights corresponding to Williams Flats fires from August 03 to August 8, 2019. FRP values from aircraft in situ observations in almost all cases are higher than RAVE FRP values. The large discrepancies are associated with missed fire detections or detections that missed the hottest part of the fire front (flaming). Because fire emissions are directly dependent on the magnitude of FRPs, it can be concluded that RAVE fire emissions are underestimated.

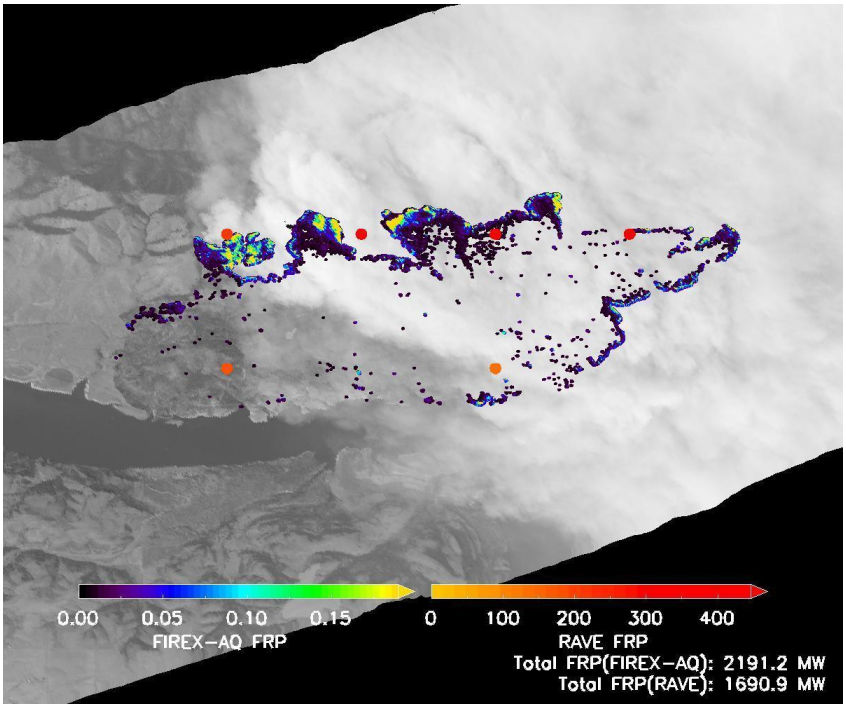

Figure 8. MODIS airborne simulator observations of FRPs on August 3, 2019 clearly showing the fire front. Overlaid in orange colored circles are RAVE FRPs

Table 4: Comparison of RAVE FRPs with FIREX-AQ aircraft observations

Date	Time (UTC)	FIREX-AQ	RAVE	No. of ABI Pixels	% Difference (FIREX-AQ – RAVE)
August 3, 2019	2151_2159	2191.2	1690.9	6	23
August 3, 2019	2220_2223	896.1	910.7	3	-1.6
August 4, 2019	0020_0023	3383.2	460.4	2	86
August 4, 2019	0034_0037	993.9	449.7	2	55
August 6, 2019	2153_2156	767.1	533.1	4	31
August 7, 2019	2315_2317	9265.3	2244.8	5	76
August 8, 2019	0055_0103	12976.8	5936.5	7	54
August 8, 2019	0232_0238	6355.1	2074.8	3	67

When we compared RAVE CO emissions with TROPOMI CO, however, the agreement was better. However, the fires in this comparison study are small fires with distinct plume boundaries and no cloud cover and correspond to different times of the year (2020 and 2021) and different biomass types. Over the 27 fires, the total mass of the FRP-based RAVE CO varied from 0.12 to 9.56 Gg, which is similar to the range (0.15 – 9.48 Gg) of TROPOMI CO. The RAVE CO and TROPOMI CO are significantly correlated ($R2=0.94$, $p < 0.001$), with a root mean square error (RMSE) of 0.56. Overall, the RAVE CO, on average, is 11% (22% at a 95% confidence interval) higher than TROPOMI CO (Figure 9). The TROPOMI CO based validation practice is also undergoing over individual fire events occurred in 2020-2021 fire seasons across high-latitude

North America. Validation results will be combined with the CONUS results and be updated here soon.

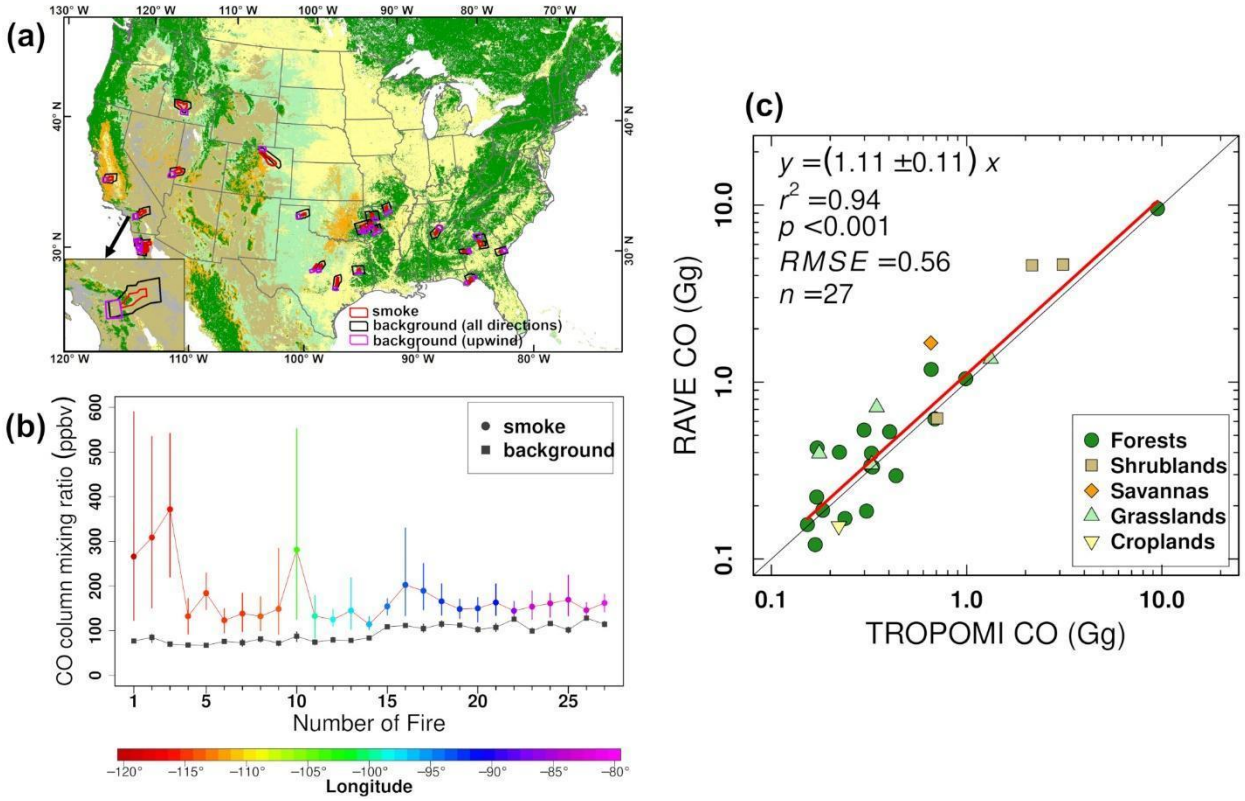

Figure 9. Comparison of CO emissions in the selected fires. (a) Distribution of the selected 27 fires overlain on the land cover map (as in Figure 1a). The inset shows a fire example. Red, black, and purple polygons delineate TROPOMI CO observations in smoke plume and background. (b) The TROPOMI CO column mixing ratio of smoke plume and upwind background in the selected fires (colored by longitude), with their mean values denoted by circles and squares, respectively. Error bars show the 20th and 80th percentile CO column mixing ratios. (c) Comparison of RAVE and TROPOMI CO mass in the selected fires.

3. Assumptions & Limitations

3.1. Performance Assumptions

None

3.2. Potential Improvements

The RAVE FRPs will be assessed further and if they are believed to be leading to under-estimation of fire emissions, we will introduce scaling factors to adjust the emissions. Though RAVE CO emissions agree with TROPOMI, the fire emissions have to be assessed over a longer

time period covering different fire regimes and seasons. For this, the RAVE science team will work with the primary user, the NWS/NCEP/EMC. EMC is currently using RAVE emissions for 2022 to conduct model simulations of aerosols. EMC model outputs of aerosol optical depth will be collected and compared to satellite observations of aerosol optical depth to determine new scaling factors for aerosol emission species.

4. References

Akagi, S.K., Yokelson, R.J., Wiedinmyer, C., Alvarado, M.J., Reid, J.S., Karl, T., Crounse, J.D., & Wennberg, P.O. (2011). Emission factors for open and domestic biomass burning for use in atmospheric models. Atmos. Chem. Phys., 11, 4039-4072, https://doi.org/10.5194/acp-11-4039-2011.

Andela, N., Morton, D.C., Giglio, L., Paugam, R., Chen, Y., Hantson, S., van der Werf, G.R., & Randerson, J.T. (2019). The Global Fire Atlas of individual fire size, duration, speed and direction. Earth Syst. Sci. Data, 11, 529-552, https://doi.org/10.5194/essd-11-529-2019.

Andreae, M.O. (2019). Emission of trace gases and aerosols from biomass burning – an updated assessment. Atmos. Chem. Phys., 19, 8523-8546, https://doi.org/10.5194/acp-19-8523-2019.

Cao, C., Luccia, F.J.D., Xiong, X., Wolfe, R., & Weng, F. (2014). Early On-Orbit Performance of the Visible Infrared Imaging Radiometer Suite Onboard the Suomi National Polar-Orbiting Partnership (S-NPP) Satellite. Ieee Transactions on Geoscience and Remote Sensing, 52, 1142-1156, https://doi.org/10.1109/TGRS.2013.2247768.

Christian, T.J., Kleiss, B., Yokelson, R.J., Holzinger, R., Crutzen, P.J., Hao, W.M., Saharjo, B.H., & Ward, D.E. (2003). Comprehensive laboratory measurements of biomass-burning emissions: 1. Emissions from Indonesian, African, and other fuels. Journal of Geophysical Research: Atmospheres, 108, https://doi.org/10.1029/2003JD003704.

Csiszar, I., Schroeder, W., Giglio, L., Ellicott, E., Vadrevu, K.P., Justice, C.O., & Wind, B. (2014). Active fires from the Suomi NPP Visible Infrared Imaging Radiometer Suite: Product status and first evaluation results. Journal of Geophysical Research: Atmospheres, 119, 2013JD020453, https://doi.org/10.1002/2013JD020453.

Darmenov, A.S., & Silva, A.d. (2015). The Quick Fire Emissions Dataset (QFED): Documentation of versions 2.1, 2.2 and 2.4. In R.D. Koster (Ed.), Technical Report Series on Global Modeling and Data Assimilation (p. 212): NASA

Friedl, M.A., Sulla-Menashe, D., Tan, B., Schneider, A., Ramankutty, N., Sibley, A., & Huang, X. (2010). MODIS Collection 5 global land cover: Algorithm refinements and characterization of new datasets. Remote Sensing of Environment, 114, 168-182, https://doi.org/10.1016/j.rse.2009.08.016.

Fu, Y., Li, R., Wang, X., Bergeron, Y., Valeria, O., Chavardès, R.D., Wang, Y., & Hu, J. (2020). Fire Detection and Fire Radiative Power in Forests and Low-Biomass Lands in Northeast Asia: MODIS versus VIIRS Fire Products. Remote Sensing, 12, 2870, https://doi.org/10.3390/rs12182870.

Giglio, L. (2007). Characterization of the tropical diurnal fire cycle using VIRS and MODIS observations. Remote Sensing of Environment, 108, 407-421, https://doi.org/10.1016/j.rse.2006.11.018.

Ichoku, C., & Ellison, L. (2014). Global top-down smoke-aerosol emissions estimation using satellite fire radiative power measurements. Atmos. Chem. Phys., 14, 6643-6667, 10.5194/acp-14-6643-2014.

Kaiser, J.W., Heil, A., Andreae, M.O., Benedetti, A., Chubarova, N., Jones, L., Morcrette, J.J., Razinger, M., Schultz, M.G., Suttie, M., & van der Werf, G.R. (2012). Biomass burning emissions estimated with a global fire assimilation system based on observed fire radiative power. Biogeosciences, 9, 527-554, https://doi.org/10.5194/bg-9-527-2012.

Kremens, R.L., Dickinson, M.B., & Bova, A.S. (2012). Radiant flux density, energy density and fuel consumption in mixed-oak forest surface fires. International Journal of Wildland Fire, 21, 722-730, https://doi.org/10.1071/WF10143.

Li, F., Zhang, X., & Kondragunta, S. (2020a). Biomass Burning in Africa: An Investigation of Fire Radiative Power Missed by MODIS Using the 375 m VIIRS Active Fire Product. Remote Sensing, 12, 1561, https://doi.org/10.3390/rs12101561.

Li, F., Zhang, X., & Kondragunta, S. (2021a). Highly anomalous fire emissions from the 2019–2020 Australian bushfires. Environmental Research Communications, https://doi.org/10.1088/2515-7620/ac2e6f.

Li, F., Zhang, X., Kondragunta, S., & Csiszar, I. (2018a). Comparison of Fire Radiative Power Estimates From VIIRS and MODIS Observations. Journal of Geophysical Research: Atmospheres, 123, 4545-4563, https://doi.org/10.1029/2017JD027823.

Li, F., Zhang, X., Kondragunta, S., & Lu, X. (2020b). An evaluation of advanced baseline imager fire radiative power based wildfire emissions using carbon monoxide observed by the Tropospheric Monitoring Instrument across the conterminous United States. Environmental Research Letters, 15, 094049, https://doi.org/10.1088/1748-9326/ab9d3a.

Li, F., Zhang, X., Kondragunta, S., & Roy, D.P. (2018b). Investigation of the Fire Radiative Energy Biomass Combustion Coefficient: A Comparison of Polar and Geostationary Satellite Retrievals Over the Conterminous United States. Journal of Geophysical Research: Biogeosciences, 123, 722-739, https://doi.org/10.1002/2017JG004279.

Li, F., Zhang, X., Kondragunta, S., Schmidt, C.C., & Holmes, C.D. (2020c). A preliminary evaluation of GOES-16 active fire product using Landsat-8 and VIIRS active fire data, and ground-based prescribed fire records. Remote Sensing of Environment, 237, 111600, https://doi.org/10.1016/j.rse.2019.111600.

Li, F., Zhang, X., Roy, D.P., & Kondragunta, S. (2019). Estimation of biomass-burning emissions by fusing the fire radiative power retrievals from polar-orbiting and geostationary satellites across the conterminous United States. Atmospheric Environment, 211, 274-287, https://doi.org/10.1016/j.atmosenv.2019.05.017.

Li, Y., Tong, D., Ma, S., Zhang, X., Kundragunta, S., Li, F., & Saylor, R. (2021b). Dominance of Wildfires Impact on Air Quality Exceedances during the 2020 Record-Breaking Wildfire

Season in the United States. Geophysical Research Letters, e2021GL094908, https://doi.org/10.1029/2021GL094908.

Liu, X., Huey, L.G., Yokelson, R.J., Selimovic, V., Simpson, I.J., Müller, M., Jimenez, J.L., Campuzano-Jost, P., Beyersdorf, A.J., Blake, D.R., Butterfield, Z., Choi, Y., Crounse, J.D., Day, D.A., Diskin, G.S., Dubey, M.K., Fortner, E., Hanisco, T.F., Hu, W., King, L.E., Kleinman, L., Meinardi, S., Mikoviny, T., Onasch, T.B., Palm, B.B., Peischl, J., Pollack, I.B., Ryerson, T.B., Sachse, G.W., Sedlacek, A.J., Shilling, J.E., Springston, S., St. Clair, J.M., Tanner, D.J., Teng, A.P., Wennberg, P.O., Wisthaler, A., & Wolfe, G.M. (2017). Airborne measurements of western U.S. wildfire emissions: Comparison with prescribed burning and air quality implications. Journal of Geophysical Research: Atmospheres, 122, 6108-6129, https://doi.org/10.1016/10.1002/2016JD026315.

Lu, X., Zhang, X., Li, F., & Cochrane, M.A. (2019). Investigating Smoke Aerosol Emission Coefficients using MODIS Active Fire and Aerosol Products — A Case Study in the CONUS and Indonesia. Journal of Geophysical Research: Biogeosciences, 0, https://doi.org/10.1016/10.1029/2018jg004974.

McCarley, T.R., Hudak, A.T., Sparks, A.M., Vaillant, N.M., Meddens, A.J.H., Trader, L., Mauro, F., Kreitler, J., & Boschetti, L. (2020). Estimating wildfire fuel consumption with multitemporal airborne laser scanning data and demonstrating linkage with MODIS-derived fire radiative energy. Remote Sensing of Environment, 251, 112114, https://doi.org/10.1016/j.rse.2020.112114.

Mota, B., & Wooster, M.J. (2018). A new top-down approach for directly estimating biomass burning emissions and fuel consumption rates and totals from geostationary satellite fire radiative power (FRP). Remote Sensing of Environment, 206, 45-62, https://doi.org/10.1016/j.rse.2017.12.016.

Prichard, S.J., O'Neill, S.M., Eagle, P., Andreu, A.G., Drye, B., Dubowy, J., Urbanski, S., & Strand, T.M. (2020). Wildland fire emission factors in North America: synthesis of existing data, measurement needs and management applications. International Journal of Wildland Fire, 29, 132-147, https://doi.org/10.1071/WF19066.

Pyne, S.J., Andrews, P.L., & Laven, R.D. (1996). Introduction to wildland fire. John Wiley and Sons

Schmidt, C.C., Hoffman, J., & Prins, E.M. (2012). GOES-R Advanced Baseline Imager (ABI) Algorithm Theoretical Basis Document For Fire / Hot Spot Characterization Version 2.5. In (pp. 1-97): NOAA NESDIS STAR

Schmit, T.J., Griffith, P., Gunshor, M.M., Daniels, J.M., Goodman, S.J., & Lebair, W.J. (2017). A Closer Look at the ABI on the GOES-R Series. Bulletin of the American Meteorological Society, 98, 681-698, https://doi.org/10.1016/10.1175/bams-d-15-00230.1.

Schroeder, W., Oliva, P., Giglio, L., & Csiszar, I.A. (2014). The New VIIRS 375 m active fire detection data product: Algorithm description and initial assessment. Remote Sensing of Environment, 143, 85-96, https://doi.org/10.1016/10.1016/j.rse.2013.12.008.

Schroeder, Giglio, L., Csiszar, I.A., & Tsidulko, M. (2020). VIIRS Active Fire Algorithm Theoretical Basis Document, available at:

https://www.star.nesdis.noaa.gov/jpss/documents/ATBD/ATBD_Iband_ActiveFires_v1.0.pdf, last access on 12/1/2021.

Wooster, M.J., Roberts, G., Perry, G.L.W., & Kaufman, Y.J. (2005). Retrieval of biomass combustion rates and totals from fire radiative power observations: FRP derivation and calibration relationships between biomass consumption and fire radiative energy release. Journal of Geophysical Research-Atmospheres, 110, D24311, https://doi.org/10.1016/10.1029/2005jd006318.

Zhang, X., Kondragunta, S., Ram, J., Schmidt, C., & Huang, H.-C. (2012). Near-real-time global biomass burning emissions product from geostationary satellite constellation. Journal of Geophysical Research-Atmospheres, 117, D14201, https://doi.org/10.1029/2012jd017459.

END OF DOCUMENT